Check for updates

Influence of morphology and heterostructure formation on the NO₂ gas sensing properties of the ZnO-NiO system

Julia Coelho Tagliaferro , Amanda Akemy Komorizono , Natalia Candiani Simões Pessoa , Rayssa Silva Correia , Maria Ines Basso Bernardi , Valmor Roberto Mastelaro *

Institute of Physics of São Carlos, University of São Paulo, 13566-590, São Carlos, SP, Brazil

ABSTRACT

The detection of toxic gases has gained significant attention in recent decades. Among various gas-sensing materials, metal oxide semiconductors (MOS) have emerged as highly promising due to their exceptional physical and chemical properties. However, a major limitation of MOS-based gas sensors is their lack of specificity, as they often respond to multiple gases, complicating the identification of target gases in mixed environments. This challenge can be addressed by combining two or more MOS materials to form a heterojunction, which modifies the electronic structure and enhances selectivity. NiO, a p-type semiconductor, has demonstrated the ability to improve both selectivity and sensor response when combined with ZnO, an n-type semiconductor. In this study, ZnO particles were synthesized via a precipitation method to produce two distinct morphologies: needle- and donut-like. These ZnO particles were subsequently combined with NiO via a hydrothermal reaction to form an n-p heterojunction. The selectivity of the resulting sensors was evaluated against O₃, NO₂, NH₃, and CO gases. The results indicated that ZnO sensors with needle- and donut-like morphologies exhibited high responses to oxidizing gases but lacked adequate selectivity between them. In contrast, the ZnO/NiO donut-like heterostructure demonstrated high selectivity for NO₂ detection.

1. Introduction

The detection of toxic gases has become increasingly important due to advancements in industrialization. Industrial and automobile emissions of gases, such as CO, O_3, NO_2, and NH_3 pose intoxication risks, even at low concentrations and short exposure durations [1]. The Occupational Safety and Health Administration (OSHA) has established exposure limits of 0.1 ppm, 5, 50, and 25 ppm for O_3, NO_2, CO, and NH_3, respectively, over an 8 h work shift. Prolonged exposure to these gases can lead to various health complications, such as irritation of the eyes, throat, and lungs, hypoxia, tissue damage, and, in severe cases, death [2–4]. Therefore, there is a pressing need to develop gas sensors with rapid response times, high sensitivity, and selectivity, even at low concentrations.

Different classes of materials have been used as gas sensors, including polymers [5,6], carbon nanotubes [7,8], carbon and graphene nanoparticles [9–11], and metal oxide semiconductors (MOS) [12–14]. Among these, MOS have demonstrated superior sensing characteristics in terms of response time and sensitivity to different gases, along with

low production costs and straightforward synthesis processes [13]. Despite these advantages, MOS-based sensors typically show low selectivity and high operating temperatures ranging from 150 to 400 °C [14].

Commonly studied MOS include SnO_2 [15,16], WO_3, In_2O_2 [17], and ZnO [18], the latter of which is an n-type semiconductor widely investigated for gas sensing due to its excellent physical, thermal, and chemical properties. ZnO possesses a high energy bandgap, high electron mobility, and outstanding thermal and chemical stability. It can be synthesized in various morphologies through methods such as precipitation [19], hydrothermal reaction [20,21], and sol-gel techniques [22], among others. Moreover, ZnO can be doped with other metals [19,23] or combined with other materials, including semiconductor oxides and graphene [11,24], to form heterojunctions.

Current research focuses on improving the selectivity and lowering the operating temperature of MOS-based gas sensors. These improvements can be achieved through morphology modification [25,26], doping [27,28], or more prominently, the formation of heterostructures between two or more different materials [29,30]. Carefully designed

---

heterostructures, incorporating considerations such as material selection, morphology, and interface engineering, enable the development of gas sensors with tailored selectivity for the detection of target gases, making heterojunctions a powerful tool for developing highly selective gas sensors [29]. Heterostructures are formed by direct contact between two or more different semiconductors at the microscopic level and are divided into three types: n-p (or p-n), p-p, and n-n. Among these, n-p heterostructures have been extensively studied and have demonstrated superior response, selectivity, and recovery times compared to their isolated constituents [29]. The formation of a heterojunction facilitates charge-carrier transfer to achieve equilibrium of the Fermi level at the heterojunction interface [31]. Depending on the morphology and band alignment, heterojunctions can have a complex effect on gas sensor behavior, particularly concerning selectivity [31]. At the heterojunction interface, the charge carriers shift until equilibrium is achieved, forming a built-in electric field. This field can attract or repel specific gas molecules, thereby enhancing the sensor's response to particular gases. For instance, p-n heterojunctions, formed between p-type and n-type semiconductors, can be tailored to respond differently to oxidizing and reducing gases [31–35]. Heterojunctions can also increase the number of oxygen vacancies, which act as active sites for gas adsorption. It has been shown that vacancies increase the sensitivity to gases that strongly interact with these vacancies, thereby improving selectivity [32]. While p-p and n-n heterojunctions have also shown promising results [34–37], n-p and p-n heterostructures consistently deliver superior results [29, 38].

In this study, ZnO was synthesized by a controlled precipitation method to produce two different morphologies: thin, elongated, solid shapes, termed "needles," and spheroid, porous, hollow particles, referred to as "donuts." The addition of a second metallic oxide affects the surface and electronic properties, such as resistance modulation, adsorption, and reactivity, thereby improving sensor properties, including selectivity. A hydrothermal process was employed to form a heterojunction between ZnO needles and donut particles with NiO nanoparticles. Sensors based on pure ZnO and ZnO/NiO heterostructures with different morphologies were tested for oxidizing (O_3 and NO_2) and reducing gases (NH_3 and CO) to evaluate their selectivity. The results revealed that pure ZnO sensors exhibited high sensitivity to oxidizing gases but lacked adequate selectivity. In contrast, the ZnO/NiO donut-based heterostructure sensors showed high sensitivity and selectivity for NO_2. These results suggest that forming an n-p-type heterostructure with specific morphology significantly improves the selectivity of the gas sensors.

2. Materials and methods

2.1. Synthesis of ZnO particles

To synthesize needle-like ZnO particles, a 0.3 M zinc acetate solution was stirred constantly at 1200 rpm at room temperature. Ammonium hydroxide was gradually added until the pH of the mixture reached 8.8. The precipitate was allowed to rest undisturbed for eight days to promote nucleation and crystal growth. Subsequently, it was collected, washed, and redispersed four times in distilled water. The final product underwent drying at 80 °C and thermal treatment at 300 °C for 2 h to remove impurities [39].

For donut-like morphology, synthesis was conducted at 100 °C. A 0.15 M zinc acetate solution in ethanol was stirred magnetically while ammonium hydroxide was slowly added until the pH reached 8.0. The processes of aging, washing, drying, and annealing were identical to those used for the needle-like morphology, yielding light-gray ZnO powder [39].

2.2. Synthesis of ZnO/NiO heterostructures

The Heterostructures were synthesized following the method reported by Lu et al. [40]. For the needle-like ZnO/NiO heterostructure, 80 mg of the pre-prepared ZnO powder was mixed with 25 mg of nickel chloride ($NiCl_2$), 20 ml of ethanol, and 40 ml of deionized water. The mixture was homogenized under magnetic stirring and then transferred to a Teflon container. The container was placed in a hydrothermal reactor and maintained at 120 °C for 10 h. The resulting precipitate was collected and washed four times (twice with deionized water and twice with ethanol). Finally, the product was dried at 60 °C and annealed at 500 °C for 2 h.

For the donut-like ZnO/NiO heterostructure, 40 mg of ZnO powder was mixed with 25 mg of $NiCl_2$, 10 ml of ethanol, and 20 ml of deionized water under magnetic stirring and then transferred to a Teflon container, which was also kept at 120 °C for 10 h. After the hydrothermal reaction, the precipitate was collected, washed with water and ethanol, dried, and annealed at 500 °C for 2 h [40]. The ratio of ZnO to $NiCl_2$ for each morphology was optimized through several tests to achieve the desired microstructure.

2.3. Material characterization

X-ray diffraction (XRD) data were obtained using a Rigaku Ultima IV diffractometer equipped with a Cu target and Cu-Kα radiation (λ =1.5418 nm). Data were collected for angles ranging from 20 to 80 °. X-ray photoelectron spectroscopy (XPS) measurements were performed with a Scienta Omicron ESCA spectrometer using an Al-Kα monochromatic X-ray source. Spectra were calibrated to the carbon component (284.8 eV), and peak fitting was conducted with Casa-XPS software.

Scanning electron microscopy (SEM) was carried out using a ZEISS SIGMA electron microscope with an FEG electron gun, and transmission electron microscopy (TEM) was conducted using an FEI TECNAI G^2 F20 high-resolution transmission electron microscopy (HRTEM) operating at 200 kV. TEM capabilities included high-resolution imaging, dark and light field imaging, and energy-dispersive X-ray spectroscopy (EDS) analysis.

The surface areas of the samples were measured using the Brunauer-Emmett-Teller (BET) technique with a Micromeritics ASAP-2020 instrument. The samples were degassed at 70 °C for 24 h and cooled to 77 K for measurements.

2.4. Detection of toxic gases

The sensors were fabricated on a silicon substrate with interdigitated Pt electrodes. A film was prepared by drop-casting five layers of a 10 mg/mL water suspension of ZnO and ZnO/NiO particles onto the electrodes, followed by sintering at 400 °C for 2 h.

O_3 gas was generated by exposing dry synthetic air to UV radiation (lamp UVP P/N 90-0004-01) at a flow rate of 100 ccm, with concentrations verified by a commercial gas sensor (TI F123513-00-1388) between 30 ppb and 370 ppb. Permeation tubes generated NO_2 and NH_3 gases in an OVG system maintained at a 100 ccm flux. Finally, CO was obtained from a pressurized cylinder, and the concentrations varied by mixing dry synthetic air with pure CO at a flux of 100 cm.

The electrical resistance was measured by calculating the ratio of the electrical current, measured using a Keithley 6514 electrometer, and a 1 V voltage applied by a Tektronix PWS4205 source to the electrodes. The substrates were placed on a PID-controlled hot plate with a thermocouple attached close to the sample to ensure accurate temperature readings during gas-sensing tests.

The sensor response for n-type semiconductor was calculated as (R_g-R_0)/$R_0 \times 100\%$ [13], where R_g is the electrical resistance in the presence of O3, and R_0 is the resistance in dry air.

3. Results and discussion

3.1. Structural characterization

Fig. 1 shows the XRD patterns of the ZnO and ZnO/NiO samples compared with the reference files JCPDS: 36-1451 (ZnO) and JCPDS# 04-0835 (NiO). The ZnO particles exhibited 11 characteristic peaks between 20° and 80°, consistent with the wurtzite crystal structure expected for ZnO under ambient conditions [39]. For the ZnO/NiO heterojunctions, peaks corresponding to the NiO phase with a rock salt structure [40] were anticipated. However, diffraction angles of the (111), (220), and (311) planes of the NiO phase closely aligned with the (101), (103), and (202) planes of the ZnO phase. Consequently, only the low-intensity peak related to the (200) plane of the NiO phase was visible due to the relatively small amount of NiO compared to ZnO.

The peak corresponding to the (002) plane in the XRD patterns of ZnO showed a higher intensity across all samples, indicating a preferential growth direction of ZnO along the c-axis, which corresponds to the [0001] crystallographic direction. The absence of peaks related to other phases confirmed the high purity of the ZnO and ZnO/NiO crystals.

3.2. Surface and morphological characterization

The surface morphologies of the ZnO and ZnO/NiO particles were investigated using SEM. As shown in Fig. 2(a), the needle-like ZnO particles displayed an elongated shape with faceted surfaces formed by layer stacking along the [0001] crystallographic direction [39]. In contrast, Fig. 2(b) illustrates the donut-shaped ZnO particles, characterized by their round, porous, and hollow structure with a central cavity. Using ImageJ software, the particles' diameter, thickness, and length were measured, and their average size distributions are shown in Fig. 2(c)–(f). The average length of ZnO needles was 6.0 μm with an average diameter of 0.3 μm, whereas ZnO donuts had an average diameter of 0.4 μm and a thickness of 0.2 μm. Aspect ratios, calculated as the ratio of particle length to thickness, were determined to be 19,0 for needle-like particles and 2.3 for donut-shaped particles.

The formation of these distinct morphologies can be explained by the basic medium in which the chemical reactions occur. For the ZnO needle-like nanoparticles, the addition of ammonium hydroxide led to the adsorption of the anionic precursor ($[Zn(OH)_4]_{2-}$) on the positively charged face of the crystal ([0001] – c-axis), promoting anisotropic growth along this direction. The synthesis of ZnO donut nanoparticles occurred at 100 °C, above the boiling point of ethanol (78.4 °C), where the porous surface likely resulted from the rapid evaporation of the solvent during the process. The central cavity is attributed to pressure differentials between the external and internal surfaces of the particles, causing inward deformation of the particle wall [39].

Fig. 2(g) illustrates the magnified SEM image of the ZnO/NiO needles, revealing porous nanosheets composed of NiO formed on the faceted surface of the original ZnO needle particles during the hydrothermal reaction. Similarly, Fig. 2(h) shows the formation of spherical NiO nanoparticles adhered to the surfaces of the ZnO donuts.

The surface area of the samples was determined using the BET technique. The ZnO needles had a surface area of 1.8 m^2/g, whereas the ZnO donuts had a larger surface area of 7.1 m^2/g. This difference can be ascribed to particle size variation, porosity, and aspect ratios [41–43]. The surface areas for the ZnO/NiO heterostructures were reduced to 0.9 m^2/g for ZnO/NiO needles and 5.3 m^2/g for ZnO/NiO donuts.

TEM measurements were performed on the heterostructured samples to confirm whether the NiO nanoparticles were in direct contact with the ZnO surface. HRTEM images, shown in Fig. A(1)–(2) and A(6)–(7) in the supplementary material, enabled the measurement of the interplanar distance between the NiO crystal planes using ImageJ software for ZnO/NiO. The interplanar distance was found to be 0.21 nm for both morphologies, consistent with previous reports [40]. The EDS results, shown in Fig. A(3–5) for the ZnO needles and A(8–10) of the ZnO donuts, reveal that the samples consist of ZnO particles in their original morphology, with NiO nanoparticles adhered to their surfaces.

3.3. Chemical characterization

Figure B, shown in the Supplementary Material, displays the survey spectra of the samples. Peaks corresponding to the binding energies of the C 1s, O 1s, Ni 2p, and Zn 2p orbitals were observed at 285, 530, 853, and 1021 eV, respectively. As shown in Table 1, the needle-like particles showed higher concentrations of oxygen and zinc for both ZnO and ZnO/NiO than the donut-like particles. In contrast, the ZnO/NiO donuts
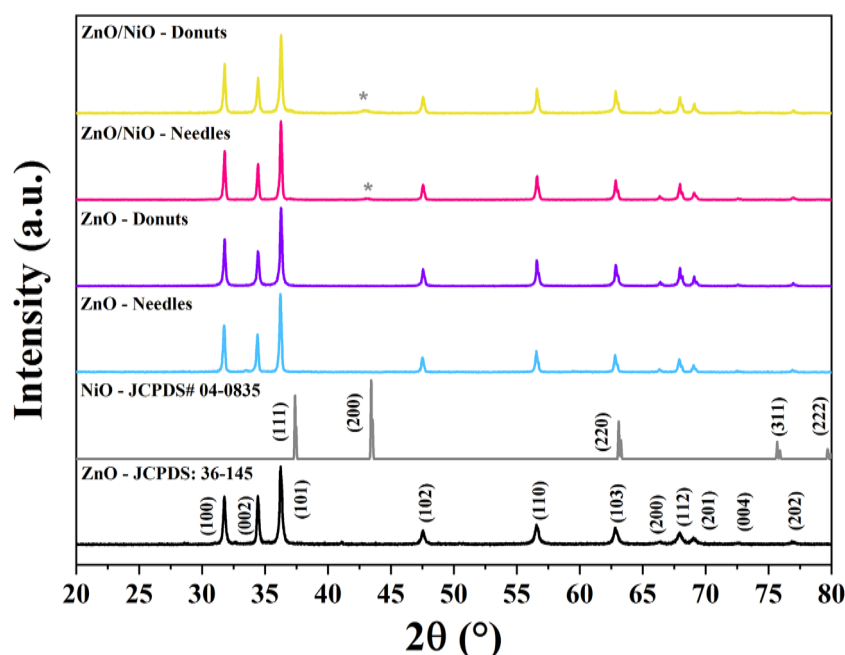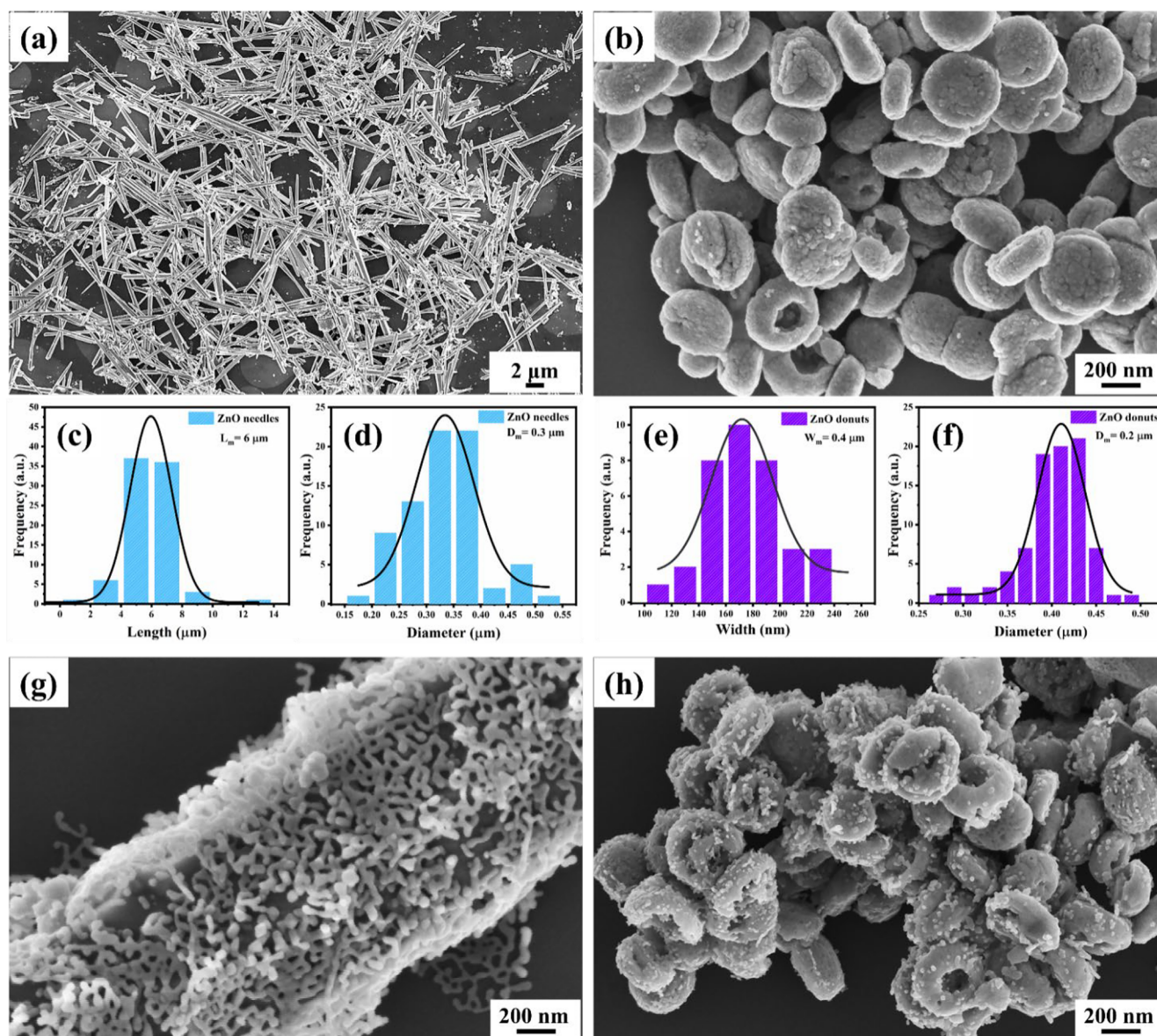

Fig. 1. X-ray diffraction patterns of ZnO needles, ZnO donuts, ZnO/NiO needles, and ZnO/NiO donuts.

Fig. 2. SEM images of (a) ZnO needles and (b) ZnO donuts, graph of the mean distribution of (c) length and (d) diameter of ZnO needles, (e) width and (f) diameter of ZnO donuts, and SEM images of the heterostructures of (g) ZnO/NiO needles and (h) ZnO/NiO donuts.

Table 1
Atomic percentages of the elements detected from the ZnO needles and donuts survey spectra and ZnO/NiO needles and donuts heterostructures.

Samples	C 1s (% at)	O 1s (% at)	Zn 2p (% at)	Ni 2p (% at)
ZnO needles	43.3	45.4	11.3	–
ZnO donuts	54.3	38.4	7.3	–
ZnO/NiO needles	48.1	43.6	7.1	1.1
ZnO/NiO donuts	57.8	35.9	3.1	3.2

have a higher Ni content, indicating that Ni atoms substituted some Zn atoms on the surface of the heterojunction.

The high-resolution O 1s orbitals of the samples, shown in Fig. 3 (a) and (b), were fitted with three components located at 530, 531, and 532 eV. The peak at 530 eV is attributed to O^{2-} species bonded to the Zn crystal lattice, whereas the peak at 531 eV is attributed to O–OH bonds [44–46]. The third peak at 532 eV is associated with functional groups chemically adsorbed onto the material's surface [47].

Four components were used to fit the experimental data for the heterostructured samples. The peaks at ~530 and ~529 eV correspond to the Zn–O and Ni–O lattice bonds, respectively [48,49], whereas the peak at ~531 eV is ascribed to adsorbed OH^- radicals bonded to NiO [50]. The peak at ~532 eV is related to adsorbed OH^- and carbon species [51].

High-resolution spectra of the Zn 2p orbitals of ZnO and ZnO/NiO, presented in Fig. C of the supplementary material, exhibit two characteristic degenerate peaks for the Zn $2p_{3/2}$ and Zn $2p_{1/2}$ levels. The binding energies for the Zn $2p_{3/2}$ orbital were 1021.5 eV for both ZnO needles and ZnO donuts, whereas those for the heterostructured samples were slightly higher, at 1021.7 eV for ZnO/NiO needles and 1021.9 eV for ZnO/NiO donuts. These values are consistent with the literature, showing a 23.1 eV energy gap between the Zn $2p_{3/2}$ and Zn $2p_{1/2}$ levels [45].

The high-resolution XPS spectra of the Ni 2p orbitals of the heterostructures, shown in Fig. 4, exhibit two degenerate peaks at 853–855 and 871–873 eV ascribed to the Ni $2p_{3/2}$ and Ni $2p_{1/2}$ levels, respectively, as well as two peaks at 861 and 879 eV related to the satellite peaks of Ni^{2+}. These satellite peaks are attributed to different energy loss
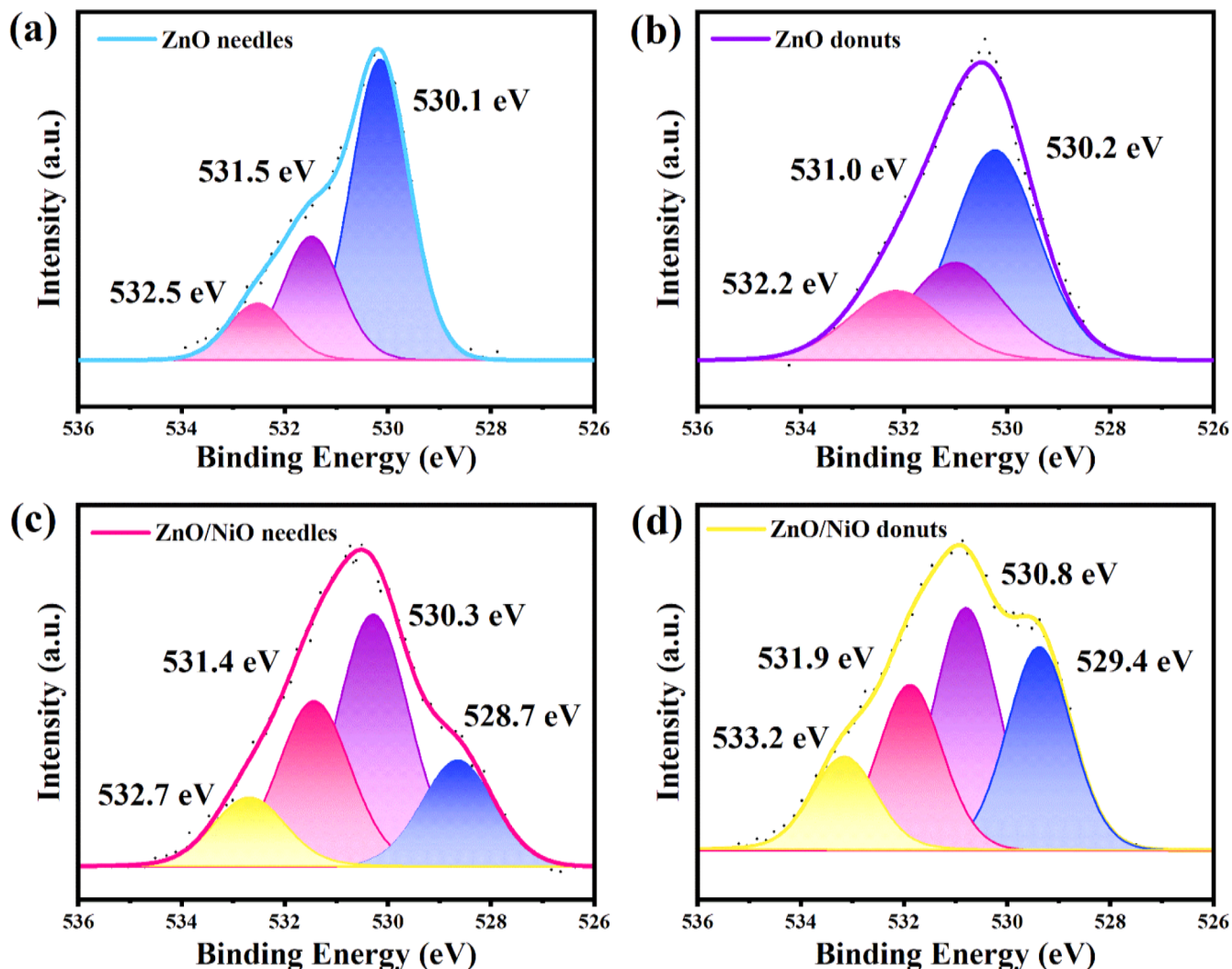
Fig. 3. High-resolution O 1s spectra for (a) ZnO needles, (b) ZnO donuts, (c) ZnO/NiO needles, and (d) ZnO/NiO donuts.
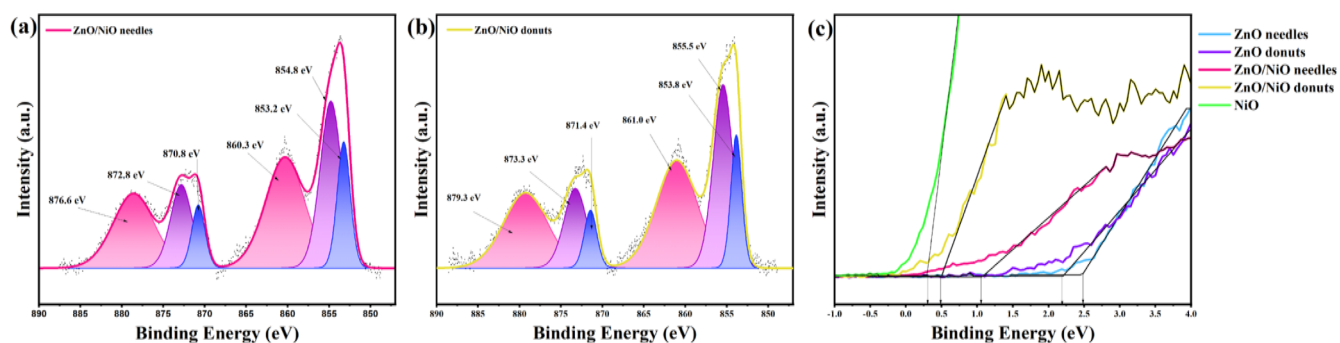

Fig. 4. High-resolution Ni 2p orbitals for (a) ZnO/NiO needles and (b) ZnO/NiO donuts, and (c) valence band maximum energy for ZnO needles, ZnO donuts, ZnO/NiO needles, and ZnO/NiO donuts.

mechanisms that produce photoelectron emissions. The peaks at 853 and 855 eV are ascribed to the Ni–O bonds in the crystal lattice, and the observed asymmetry in the spectra is related to the presence of different Ni oxidation states in the samples.

The component at 853.2 eV (Fig. 4(a)) is assigned to the Ni^{2+} oxidation state, representing 19.0% of the total bonds in the ZnO/NiO needles, whereas the peak at 854.8 eV corresponds to the Ni^{3+} oxidation state, representing 47.8% of the chemical bonds in the sample. For ZnO/

NiO donuts (Fig. 4(b)), the peak at 853.8 eV corresponds to the Ni^{2+} state, representing 19.2% of the bonds, and the peak at 855.5 eV corresponds to the Ni^{3+} state, representing 47.6% of the total chemical bonds in the sample. According to the literature, the component at 853 eV is ascribed to bonds between Ni^{2+} ions and lattice oxygen, whereas the oxygen vacancies induce the formation of Ni^{3+} ions, which can bond to -OOH species and lead to O^{2-} adsorbed molecules capturing electrons from the conduction band of the material, thus increasing the

electrochemical performance of the sensor [52].

The valence band (VB) spectra of the samples, shown in Fig. 4(c), were used to determine the VB maximum energy for the four samples (ZnO needles, ZnO donuts, ZnO/NiO needles, and ZnO/NiO donuts) and NiO. The VB energies of the ZnO needles and donuts were measured at 2.2 eV and 2.5 eV, respectively, according to the values reported in the literature [49–51]. On the other hand, the VB energies for the heterostructured samples—ZnO/NiO needles and donuts—were significantly lower at 1.1 and 0.5 eV, respectively. This reduction is attributed to the low VB energy of NiO, measured at 0.2 eV, which was used as the standard. When a heterojunction forms between two materials, their Fermi levels align, causing the bending of the valence and conduction bands to establish Fermi level equilibrium. This interaction results in a potential barrier and offsets in the valence and conduction bands. Consequently, the VB energy of heterostructured materials lies between the VB energies of pure materials [29].

3.4. Sensing performance towards ozone gas

3.4.1. ZnO needle and donut sensors

The ZnO needle and donut sensors were tested for their response to oxidizing gases (O_3 and NO_2) and reducing gases (NH_3 and CO) at different operating temperatures. The dynamic response-recovery curves for these gases at 300, 250, and 200 °C are shown in Fig. D–F of the supplementary material. Although the responses of both sensors increased as the temperature decreased, a drift in the resistance curve was observed in some cases. Fig. 5 displays the response of the ZnO needle and donut sensors to the target gases at different temperatures. For ozone (blue bar), both sensors demonstrated optimal response and stability at 200 °C. Similarly, for NO_2 (pink bar), both sensors showed better response and stability at 200 °C. Neither sensor showed sensitivity to CO and only a low sensitivity to NH_3 (purple bar) reducing gases. Specifically, when exposed to NH_3, the needle sensor showed a better response and stability at 250 °C, whereas the donut sensor provided a better response at 200 °C but exhibited significant drift on the resistance curve. These results indicate that the most substantial effect of morphology is a reduction in the optimal operating temperature for the donut sensor when exposed to ozone (200 °C).

Sensor selectivity is a critical factor in gas sensing applications, defined as the ability to detect a particular gas in the presence of other gases. The selectivity of the ZnO needle and donut sensors was evaluated for oxidizing gases (O_3 and NO_2) and reducing gases (NH_3 and CO), as shown in Fig. 6. Both sensors showed low or no response to NH_3 and CO, while their responses to O_3 and NO_2 were similar. These results suggest

that neither the ZnO needle nor the donut sensors exhibited good selectivity for the oxidizing gases.

3.4.2. ZnO/NiO heterostructured needle sensors

Fig. 7(a) and (b) display the response-recovery curves of the ZnO/NiO needle sensor exposed to O_3 at 300 and 250 °C, respectively. Due to the high electrical resistance of the sensor, measurements could not be conducted below 250 °C. At 250 and 300 °C, the sensor demonstrated sensitivity to O_3 without saturation at different exposure concentrations. Fig. 7(c) and (d) display the response-recovery curves for the ZnO/NiO needle sensor exposed to NO_2 at 300 and 250 °C. The sensor was sensitive to NO_2 at all concentrations and temperatures, with no evidence of saturation. Additionally, its response increased significantly as the temperature decreased from 300 to 250 °C. However, no change in resistance was observed when the sample was exposed to reducing gases (NH_3 and CO).

3.4.3. ZnO/NiO heterostructured donut sensors

Fig. 8 displays the response-recovery curves of the ZnO/NiO donut sensor when exposed to NO_2 at 300, 250, and 200 °C. The sensor showed good sensitivity to NO_2 at all evaluated temperatures; however, at 200 °C, it exhibited analyte saturation. Unlike the ZnO and ZnO/NiO needle sensors, the ZnO/NiO donut sensor shows a reduction in electrical resistance upon exposure to NO_2. This behavior is characteristic of p-type semiconductors such as NiO, suggesting that NiO drives chemical reactions in ZnO/NiO donut sensors, as opposed to the ZnO/NiO needle sensor [31,53]. The sensor responses are equal to 6.4, 22.6, and 37.5% for 900 ppb of NO_2 at 300, 250, and 200 °C, respectively. These results indicate that the optimal operating temperature of the sensor is 250 °C, as significant resistance drift was observed at 300 °C, while sensor saturation occurred at 200 °C. The ZnO/NiO donut sensor did not exhibit sensitivity to O_3, NH_3, or CO at any concentration or temperature.

3.4.4. Selectivity

Fig. 9 displays the responses of the ZnO needle and donut sensors and their respective heterojunctions at 250 °C to O_3 (30 ppb), NO_2 (900 ppb), NH_3 (11 ppm), and CO (10 ppm). The ZnO/NiO needle heterojunction (pink bar) demonstrated a significantly higher response to O_3 than the ZnO needle sensor (blue bar). However, its response to NO_2 gas was not substantially different from that of the ZnO needle sensor. Both heterostructured sensors showed no sensitivity to the reducing gases. A notable observation is the behavior of the heterostructured ZnO/NiO donut sensor (yellow), which showed sensitivity only to NO_2 gas. These
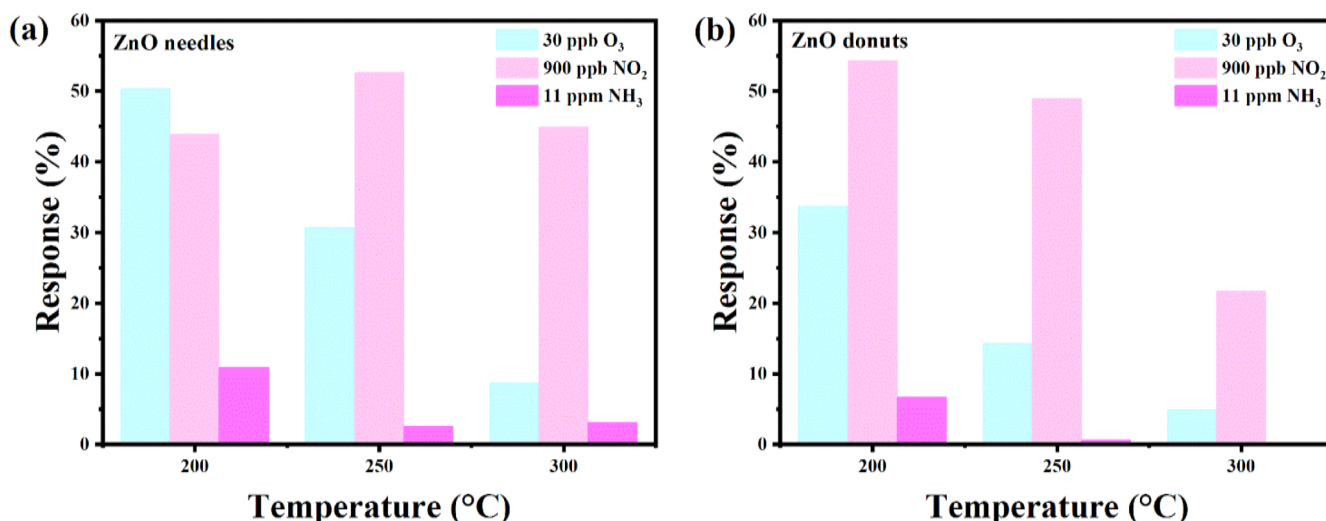

Fig. 5. Response (%) as a function of temperature for the (a) ZnO needle and (b) ZnO donut sensors.
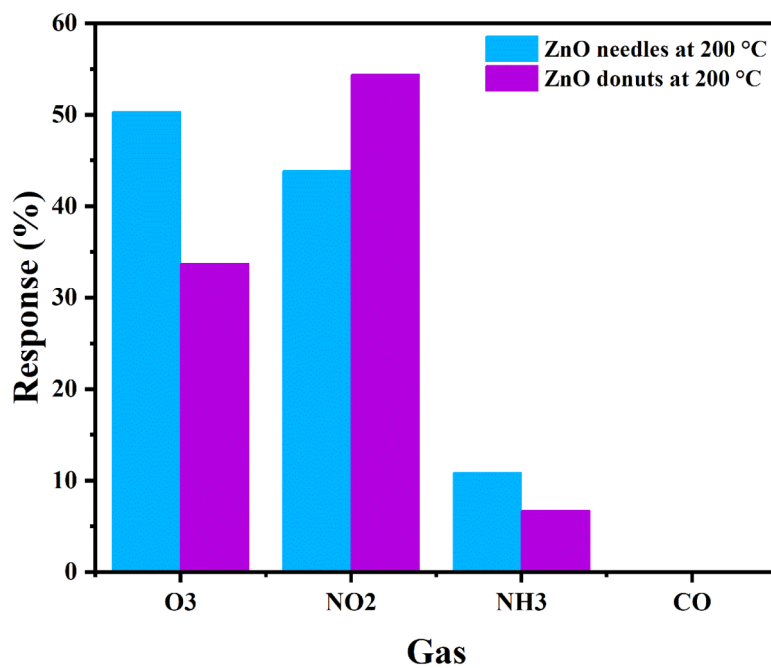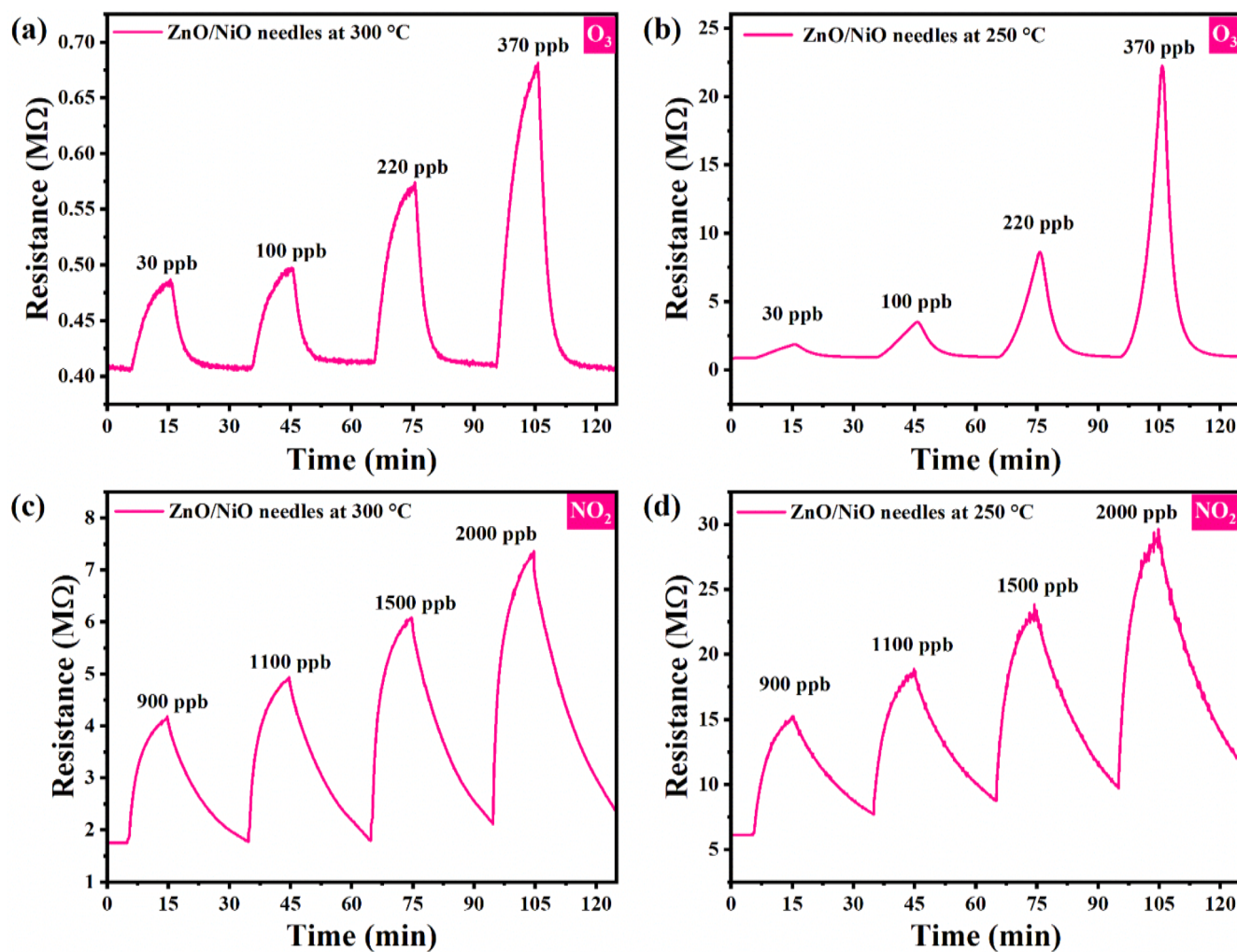
Fig. 6. Selectivity of the ZnO needle and donut sensors.

Fig. 7. Response-recovery curves of the ZnO/NiO needle sensor to O_3 at (a) 300 °C and (b) 250 °C and to NO_2 at (c) 300 °C and (d) 250 °C.
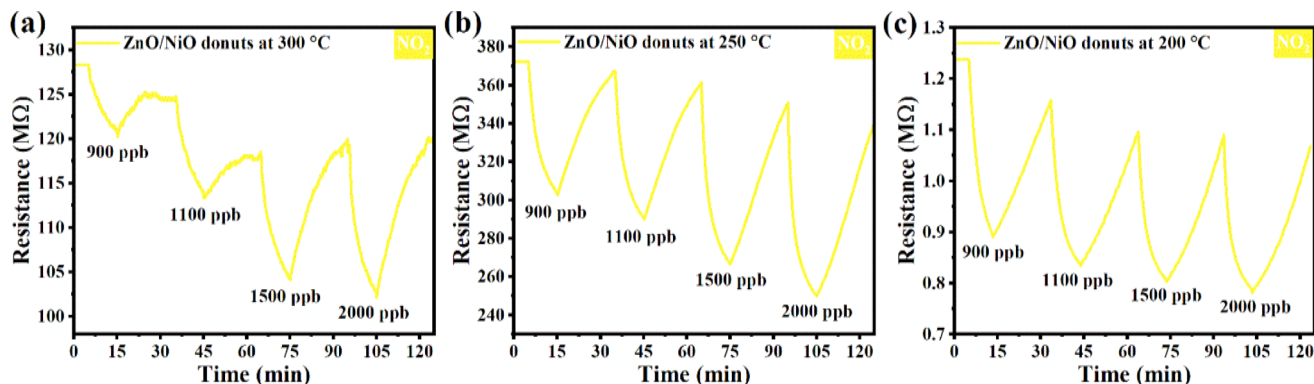
Fig. 8. Response-recovery curves of the ZnO/NiO donut sensors to NO_2 at (a) 300 °C, (b) 250 °C, and (c) 200 °C.
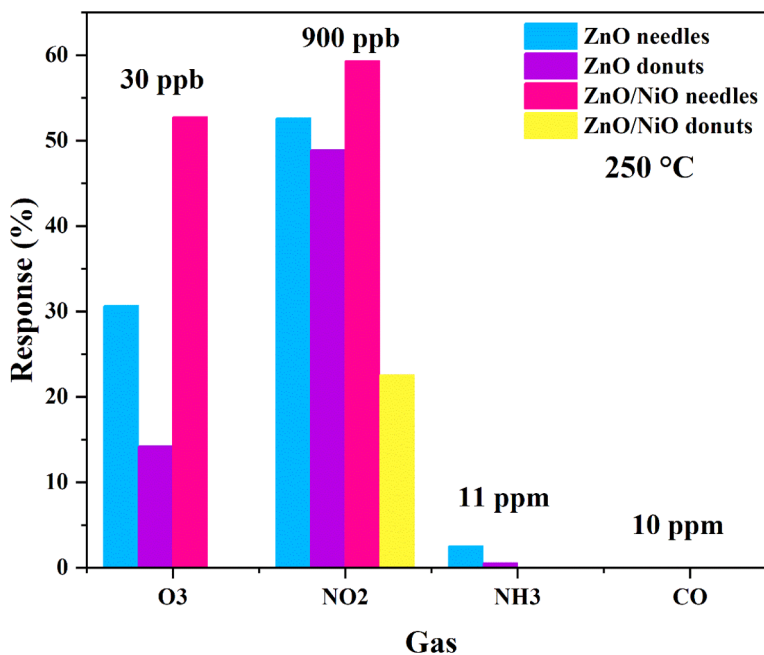

Fig. 9. Selectivity of all sensors at 250 °C.

results suggest that the heterostructured ZnO/NiO donut sensor demonstrates high selectivity for NO_2 gas, whereas the heterostructured ZnO/NiO needle sensor shows lower selectivity but a higher response to O_3.

Compared to recently reported NO_2 sensors, the ZnO/NiO exhibited a good response of 23.2% at 900 ppb of NO_2. For instance, Zhen et al. [54] synthesized $AgTe_2$ nanoparticles for NO_2 detection, achieving a response value of approximately 25% at 50% humidity and room temperature at a 1 ppm concentration. Similarly, Qiuni et al. [55] developed $Mo_2TiC_2T_x/MoS_2$ composites that exhibited high response and selectivity towards NO_2 at concentrations ranging from 2 to 50 ppm under room temperature. Additionally, Sun et al. [56] reported that a Ce-doped ZnO sensor demonstrated excellent selectivity at 250 °C when exposed to 10 ppm of NO_2.
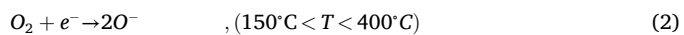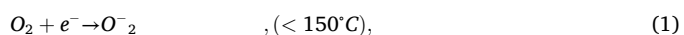
In summary, the results of this study are comparable to, or even superior to, those reported in the literature, considering the more straightforward preparation methods of the ZnO/NiO sensors and their effective response to lower concentrations of NO2 gas.

3.3. Sensing mechanism

The sensing mechanism of semiconductor metallic oxide (SMO) gas

sensors is based on oxygen adsorption/desorption. When SMOs are exposed to air at a specific temperature, oxygen molecules are chemically adsorbed onto the material's surface and capture electrons from the conduction band, forming oxygen ions [13]. Therefore, the operating temperature of such sensors significantly influences their efficiency because, at low temperatures, the number of thermally excited electrons is insufficient to facilitate the formation of reactive oxygen species. The limited active sites are also thermally stable with high adsorption energy, resulting in suboptimal sensor performance [56].

The operating temperature for MOS ranges from 100 to 450 °C, with the types of reactive oxygen species adsorbed onto the surface of the particle depending on the temperature, as described in Eqs. (1)–(3) for T < 150 °C [13]:

$$O_2 + e^- \rightarrow O^-_2 \qquad , (< 150^\circ C), \tag{1}$$

$$O_2 + e^- \rightarrow 2O^- \qquad , (150^\circ C < T < 400^\circ C) \tag{2}$$

$$O_2 + e^- \rightarrow O^{2-} \qquad , (> 400^\circ C) \tag{3}$$

In an n-type semiconductor, the electrons are captured from the conduction band of SMO by the oxygen ions, creating an electron-deficient region near the particle surface, known as the charge-
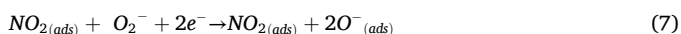
depletion region (space-charge layer). This process forms a potential barrier and induces deformation of the conduction band (Fig. G) [56]. The thickness of the space-charge layer depends on the number and type of adsorbed oxygen ions. For effective conductivity, the particle diameter must be at least double the space-charge layer thickness, and the electrons must have sufficient energy to overcome the potential barrier. 'In contrast, in p-type semiconductors, ionized oxygen species generate holes in the conduction band, forming a hole accumulation layer, a potential barrier, and band bending [13].

When an n-type sensor is exposed to an oxidizing gas (O_3), the gas molecules capture electrons from the conduction band of the material and react with the oxygen ions absorbed at the surface of the sensor, as shown in Eqs. (4) and (5) and Fig. G. This process decreases the charge carriers in the conduction band, thereby increasing the electrical resistance of the material [13,19,56]. For oxidizing gases (O_3 and NO_2) [11,57,58]:

For O_3

$$O_{3(g)} + 2e^- \rightarrow O_{2(g)} + O^-_{(ads)} \tag{4}$$

$$O_{2(g)} + 2e^- \rightarrow 2O^-_{(ads)} \tag{5}$$

For NO_2

$$NO_{2(g)} + e^- \rightarrow NO_2^-_{(g)} \tag{6}$$

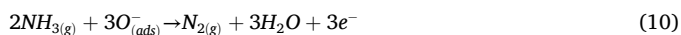$$NO_{2(ads)} + O_2^- + 2e^- \rightarrow NO_{2(ads)} + 2O^-_{(ads)} \tag{7}$$

In the presence of a reducing gas such as NH_3, the reaction between the ionized adsorbed oxygen and the gas releases surplus electrons into the conduction band (see Eqs. (8) and (9) [59–61], increasing the number of charge carriers (electrons) and decreasing electrical resistance.

For CO

$$O_{2(g)} + 2e^- \rightarrow 2O^-_{(ads)} \tag{8}$$

$$2CO_{(g)} + O_{2(ads)} \rightarrow 2CO_{2(g)} + e^- \tag{9}$$

For NH_3

$$2NH_{3(g)} + 3O^-_{(ads)} \rightarrow N_{2(g)} + 3H_2O + 3e^- \tag{10}$$

In p-type semiconductors, where charge carriers are holes, the charge transport dynamics are altered. The behavior of p-type SMO exhibits reversed characteristics compared to n-type materials. In particular, during exposure to an oxidizing gas, the electrical resistance decreases because of the increased number of charge carriers (holes) in the conduction band generated by the reaction between the target gas and adsorbed oxygen. Conversely, exposure to a reducing gas such as CO leads to the recombination of electrons from the chemical reaction and existing conduction band holes, reducing the number of charge carriers available for conduction and increasing the material's electrical resistance [13].

Charge transportation dynamics are altered in the heterostructured samples. The electrons from the n-type ZnO surface diffuse into the p-type NiO, creating a depletion layer, and a positively charged area. Meanwhile, the holes from the NiO surface diffuse into the ZnO surface, forming a hole accumulation layer and a negatively charged area. This process continues until the Fermi level of the ZnO/NiO system reaches equilibrium, resulting in a potential barrier for further charge-carrier diffusion at the n-p interface (Fig. G), which reduces conductivity and increases electrical resistance in air [38].

Depending on the target gas, the potential barrier either facilitates or impedes charge transport. For example, when the sensor is exposed to O_3 or NO_2, the latter gas gains electrons from the ZnO nanoparticles, decreasing carrier concentration and disrupting interface equilibrium. The resulting electron deficit causes holes in NiO to diffuse into ZnO until the Fermi level re-equilibrates, decreasing the heterojunction

barrier width and increasing electrical resistance. This resistance change serves as the detection signal for the gas [31,38].

4. Conclusions

The combination of precipitation and hydrothermal methods proved to be effective for synthesizing crystalline and homogeneous ZnO and ZnO/NiO samples, as confirmed by the XRD and SEM analyses. The gas detection results revealed that ZnO-based sensors exhibited a more robust response to oxidizing gases than reducing gases; however, they lacked significant selectivity among oxidizing gases across all studied morphologies. The formation of the heterostructures enhanced the selectivity of the sensors. Among the tested configurations, the ZnO/NiO heterostructured donut-shaped sensor demonstrated high selectivity for NO₂ gas, with negligible sensitivity to other oxidizing or reducing gases, highlighting its potential as an effective NO₂ sensor.

CRediT authorship contribution statement

Julia Coelho Tagliaferro: Writing – original draft, Methodology, Investigation, Formal analysis, Data curation, Conceptualization. **Amanda Akemy Komorizono:** Writing – review & editing, Validation, Investigation, Formal analysis, Data curation. **Natalia Candiani Simões Pessoa:** Investigation, Formal analysis, Data curation. **Rayssa Silva Correia:** Methodology, Investigation, Data curation. **Maria Ines Basso Bernardi:** Methodology, Investigation, Formal analysis, Conceptualization. **Valmor Roberto Mastelaro:** Supervision, Project administration, Funding acquisition, Conceptualization.

Declaration of competing interest

The authors declare that they have no known competing financial interests or personal relationships that could have appeared to influence the work reported in this paper.

Supplementary materials

Supplementary material associated with this article can be found, in the online version, at doi:10.1016/j.talo.2024.100388.

Data availability

No data was used for the research described in the article.

References

[1] Permissible Exposure Limits - Annotated Tables | Occupational Safety and Health Administration, (n.d.). https://www.osha.gov/annotated-pels (accessed October 30, 2024).

[2] S. Huang, H. Li, M. Wang, Y. Qian, K. Steenland, W.M. Caudle, Y. Liu, J. Sarnat, S. Papatheodorou, L. Shi, Long-term exposure to nitrogen dioxide and mortality: a systematic review and meta-analysis, Sci. Total Environ. 776 (2021) 145968, https://doi.org/10.1016/j.scitotenv.2021.145968.

[3] S.M. Holm, J.R. Balmes, Systematic review of ozone effects on human lung function, 2013 through 2020, Chest 161 (2022) 190–201, https://doi.org/10.1016/j.chest.2021.07.2170.

[4] Z. Chen, N. Liu, H. Tang, X. Gao, Y. Zhang, H. Kan, F. Deng, B. Zhao, X. Zeng, Y. Sun, H. Qian, W. Liu, J. Mo, X. Zheng, C. Huang, C. Sun, Z. Zhao, Health effects of exposure to sulfur dioxide, nitrogen dioxide, ozone, and carbon monoxide

between 1980 and 2019: a systematic review and meta-analysis, Indoor. Air. 32 (2022), https://doi.org/10.1111/ina.13170.

[5] X. Liu, W. Zheng, R. Kumar, M. Kumar, J. Zhang, Conducting polymer-based nanostructures for gas sensors, Coord. Chem. Rev. 462 (2022) 214517, https://doi.org/10.1016/j.ccr.2022.214517.

[6] Y.C. Wong, B.C. Ang, A. Haseeb, A.A. Baharuddin, Y.H. Wong, Conducting polymers as chemiresistive gas sensing materials: a review, J. Electrochem. Soc. 167 (2020) 037503, https://doi.org/10.1149/2.0032003JES.

[7] R.B. Onyancha, K.E. Ukhurebor, U.O. Aigbe, O.A. Osibote, H.S. Kusuma, H. Darmokoesoemo, V.A. Balogun, A systematic review on the detection and monitoring of toxic gases using carbon nanotube-based biosensors, Sens. Biosens. Res. 34 (2021) 100463, https://doi.org/10.1016/j.sbsr.2021.100463.

[8] M.N. Norizan, M.H. Moklis, S.Z.N. Demon, N.A. Halim, A. Samsuri, I.S. Mohamad, V.F. Knight, N. Abdullah, Carbon nanotubes: functionalisation and their application in chemical sensors, RSC Adv. 10 (2020) 43704–43732, https://doi.org/10.1039/D0RA09438B.

[9] S.Z.N. Demon, A.I. Kamisan, N. Abdullah, S.A.M. Noor, O.K. Khim, N.A.M. Kasim, M.Z.A. Yahya, N.A.A. Manaf, A.F.M. Azmi, N.A. Halim, Graphene-based materials in gas sensor applications: a review, Sens. Mater. 32 (2020) 759, https://doi.org/10.18494/SAM.2020.2492.

[10] W. Tian, X. Liu, W. Yu, Research progress of gas sensor based on graphene and its derivatives: a review, Appl. Sci. 8 (2018) 1118, https://doi.org/10.3390/app8071118.

[11] B.S. de Lima, A.A. Komorizono, W.A. dos S Silva, A.L. Ndiaye, J. Brunet, M.I. B. Bernardi, V.R. Mastelaro, Ozone detection in the ppt-level with rGO-ZnO based sensor, Sens. Actuators B Chem. 338 (2021) 129779, https://doi.org/10.1016/j.snb.2021.129779.

[12] S.M. Kanan, O.M. El-Kadri, I.A. Abu-Yousef, M.C. Kanan, Semiconducting metal oxide based sensors for selective gas pollutant detection, Sensors 9 (2009) 8158–8196, https://doi.org/10.3390/s91008158.

[13] A. Dey, Semiconductor metal oxide gas sensors: a review, Mater. Sci. Eng. B 229 (2018) 206–217, https://doi.org/10.1016/j.mseb.2017.12.036.

[14] P.T. Moseley, Progress in the development of semiconducting metal oxide gas sensors: a review, Meas. Sci. Technol. 28 (2017) 082001, https://doi.org/10.1088/1361-6501/aa7443.

[15] Y. Masuda, Recent advances in SnO2 nanostructure based gas sensors, Sens. Actuators B Chem. 364 (2022) 131876, https://doi.org/10.1016/j.snb.2022.131876.

[16] Z. Li, W. Zeng, Q. Li, SnO2 as a gas sensor in detection of volatile organic compounds: a review, Senso. Actuators A Phys. 346 (2022) 113845, https://doi.org/10.1016/j.sna.2022.113845.

[17] S. Yang, H. Yin, Z. Wang, G. Lei, H. Xu, Z. Lan, H. Gu, Gas sensing performance of In2O3 nanostructures: a mini review, Front. Chem. 11 (2023) 1174207, https://doi.org/10.3389/fchem.2023.1174207.

[18] M.A. Franco, P.P. Conti, R.S. Andre, D.S. Correa, A review on chemiresistive ZnO gas sensors, Sens. Actuators. Rep. 4 (2022) 100100, https://doi.org/10.1016/j.snr.2022.100100.

[19] N.S. Ramgir, K.R. Sinju, B. Bhangare, A.K. Debnath, Electronic Nose based on chemiresistive sensors for toxic gas detection, J. Mater. NanoScience 9 (2022) 79–90.

[20] G. Amin, M.H. Asif, A. Zainelabdin, S. Zaman, O. Nur, M. Willander, Influence of pH, precursor concentration, growth time, and temperature on the morphology of ZnO nanostructures grown by the hydrothermal method, J. Nanomater. 2011 (2011) 1–9, https://doi.org/10.1155/2011/269692.

[21] S. Baruah, J. Dutta, Hydrothermal growth of ZnO nanostructures, Sci. Technol. Adv. Mater. 10 (2009) 013001, https://doi.org/10.1088/1468-6996/10/1/013001.

[22] J. Lee, A.J. Easteal, U. Pal, D. Bhattacharyya, Evolution of ZnO nanostructures in sol–gel synthesis, Curr. Appl. Phys. 9 (2009) 792–796, https://doi.org/10.1016/j.cap.2008.07.018.

[23] A. Yu, J. Qian, H. Pan, Y. Cui, M. Xu, L. Tu, Q. Chai, X. Zhou, Micro-lotus constructed by Fe-doped ZnO hierarchically porous nanosheets: preparation, characterization and gas sensing property, Sens. Actuators B Chem. 158 (2011) 9–16, https://doi.org/10.1016/j.snb.2011.03.052.

[24] S.G. Chatterjee, S. Chatterjee, A.K. Ray, A.K. Chakraborty, Graphene–metal oxide nanohybrids for toxic gas sensor: a review, Sens. Actuators B Chem. 221 (2015) 1170–1181, https://doi.org/10.1016/j.snb.2015.07.070.

[25] A.C. Catto, L.F. Da Silva, C. Ribeiro, S. Bernardini, K. Aguir, E. Longo, V. R. Mastelaro, An easy method of preparing ozone gas sensors based on ZnO nanorods, RSC Adv. 5 (2015) 19528–19533, https://doi.org/10.1039/C5RA00581G.

[26] S. Wang, G. Qiao, X. Chen, X. Wang, H. Cui, Synthesis of ZnO hollow microspheres and analysis of their gas sensing properties for n-butanol, Crystals (Basel) 10 (2020) 1010, https://doi.org/10.3390/cryst10111010.

[27] K. Govardhan, A.N. Grace, Metal/metal oxide doped semiconductor based metal oxide gas sensors—A review, Sens. Lett. 14 (2016) 741–750, https://doi.org/10.1166/sl.2016.3710.

[28] S. Park, H. Kim, C. Jin, S.-W. Choi, S.S. Kim, C. Lee, Enhanced CO gas sensing properties of Pt-functionalized WO3 nanorods, Thermochim. Acta 542 (2012) 69–73, https://doi.org/10.1016/j.tca.2011.12.002.

[29] S. Yang, G. Lei, H. Xu, Z. Lan, Z. Wang, H. Gu, Metal oxide based heterojunctions for gas sensors: a review, Nanomaterials 11 (2021) 1026, https://doi.org/10.3390/nano11041026.

[30] U.T. Nakate, R. Ahmad, P. Patil, Y. Wang, K.S. Bhat, T. Mahmoudi, Y.T. Yu, E. Suh, Y.-B. Hahn, Improved selectivity and low concentration hydrogen gas sensor

[31] J. Walker, P. Karnati, S.A. Akbar, P.A. Morris, Selectivity mechanisms in resistive-type metal oxide heterostructural gas sensors, Sens. Actuators B Chem. 355 (2022) 131242, https://doi.org/10.1016/j.snb.2021.131242.

[32] J. Zhang, J. Li, The Oxygen Vacancy Defect of ZnO/NiO Nanomaterials Improves Photocatalytic Performance and Ammonia Sensing Performance, Nanomaterials 12 (2022) 433. 10.3390/nano12030433.

[33] Y. Zhang, Y. Jiang, Z. Yuan, Z. Liu, Q. Zhao, Q. Huang, Z. Li, W. Zeng, Z. Duan, H. Tai, Synergistic effect of electron scattering and space charge transfer enabled unprecedented room temperature NO2 sensing response of SnO2, Small 19 (2023) 2303631, https://doi.org/10.1002/smll.202303631.

[34] Y. Wang, F. Qu, J. Liu, Y. Wang, J. Zhou, S. Ruan, Enhanced H2S sensing characteristics of CuO-NiO core-shell microspheres sensors, Sens. Actuators B Chem. 209 (2015) 515–523, https://doi.org/10.1016/j.snb.2014.12.010.

[35] H. Gao, J. Guo, J. Li, C. Xie, X. Li, L. Liu, Y. Chen, P. Sun, F. Liu, X. Yan, Highly selective and sensitive xylene gas sensor fabricated from NiO/NiCr2O4 pp nanoparticles, Sens. Actuators B Chem. 284 (2019) 305–315, https://doi.org/10.1016/j.snb.2018.12.152.

[36] J. Zhou, M. Ikram, A.U. Rehman, J. Wang, Y. Zhao, K. Kan, W. Zhang, F. Raziq, L. Li, K. Shi, Highly selective detection of NH3 and H2S using the pristine CuO and mesoporous In2O3@ CuO multijunctions nanofibers at room temperature, Sens. Actuators B Chem. 255 (2018) 1819–1830, https://doi.org/10.1016/j.snb.2017.08.200.

[37] Y. Ding, X. Guo, B. Du, X. Hu, X. Yang, Y. He, Y. Zhou, Z. Zang, Low-operating temperature ammonia sensor based on Cu 2 O nanoparticles decorated with p-type MoS 2 nanosheets, J. Mater. Chem. C 9 (2021) 4838–4846, https://doi.org/10.1039/D1TC00391G.

[38] D. Zappa, V. Galstyan, N. Kaur, H.M.M. Arachchige, O. Sisman, E. Comini, "Metal oxide-based heterostructures for gas sensors"-a review, Anal. Chim. Acta 1039 (2018) 1–23, https://doi.org/10.1016/j.aca.2018.09.020.

[39] M. Montero-Muñoz, J.E. Ramos-Ibarra, J.E. Rodríguez-Páez, G.E. Marques, M. D. Teodoro, J.A.H. Coaquira, Growth and formation mechanism of shape-selective preparation of ZnO structures: correlation of structural, vibrational and optical properties, Phys. Chem. Chem. Phys. 22 (2020) 7329–7339, https://doi.org/10.1039/C9CP06744B.

[40] Y. Lu, Y. Ma, S. Ma, S. Yan, Hierarchical heterostructure of porous NiO nanosheets on flower-like ZnO assembled by hexagonal nanorods for high-performance gas sensor, Ceram. Int. 43 (2017) 7508–7515, https://doi.org/10.1016/j.ceramint.2017.03.032.

[41] I.E. Dubois, S. Holgersson, S. Allard, M.E. Malmström, Dependency of BET surface area on particle size for some granitic minerals, Proc. Radiochem. 1 (2011) 75–82, https://doi.org/10.1524/rcpr.2011.0013.

[42] H. Yin, P.S. Casey, Effects of aspect ratio (AR) and specific surface area (SSA) on cytotoxicity and phototoxicity of ZnO nanomaterials, Chemosphere 124 (2015) 116–121, https://doi.org/10.1016/j.chemosphere.2014.11.076.

[43] L.J. Michot, F. Villieras, Surface area and porosity, Dev. Clay. Sci. 1 (2006) 965–978, https://doi.org/10.1016/S1572-4352(05)01035-4.

[44] R. Al-Gaashani, S. Radiman, A.R. Daud, N. Tabet, Y. Al-Douri, XPS and optical studies of different morphologies of ZnO nanostructures prepared by microwave methods, Ceram. Int. 39 (2013) 2283–2292, https://doi.org/10.1016/j.ceramint.2012.08.075.

[45] M. Kwoka, A. Kulis-Kapuscinska, D. Zappa, E. Comini, J. Szuber, Novel insight on the local surface properties of ZnO nanowires, Nanotechnology 31 (2020) 465705.

[46] M. Chen, Z. Wang, D. Han, F. Gu, G. Guo, High-sensitivity NO2 gas sensors based on flower-like and tube-like ZnO nanomaterials, Sens. Actuators B Chem. 157 (2011) 565–574, https://doi.org/10.1016/j.snb.2011.05.023.

[47] S.A. Leontiev, S.V. Koshcheev, V.G. Devyatov, A.E. Cherkashin, É.P. Mikheeva, Detailed XPS and UPS studies of the band structure of zinc oxide, J. Struct. Chem. 38 (1997) 725–731, https://doi.org/10.1007/BF02763884.

[48] A. Echresh, C.O. Chey, M.Z. Shoushtari, V. Khranovskyy, O. Nur, M. Willander, UV photo-detector based on p-NiO thin film/n-ZnO nanorods heterojunction prepared by a simple process, J. Alloys. Compd. 632 (2015) 165–171, https://doi.org/10.1016/j.jallcom.2015.01.155.

[49] W.-D. Zhou, D. Dastan, J. Li, X.-T. Yin, Q. Wang, Discriminable sensing response behavior to homogeneous gases based on n-ZnO/p-NiO composites, Nanomaterials 10 (2020) 785, https://doi.org/10.3390/nano10040785.

[50] K.X. Steirer, K.L. Ou, N.R. Armstrong, E.L. Ratcliff, Critical interface states controlling rectification of ultrathin NiO–ZnO p–n heterojunctions, ACS Appl. Mater. Interfaces 9 (2017) 31111–31118, https://doi.org/10.1021/acsami.7b08899.

[51] S. Periyannan, L. Manceriu, N.D. Nguyen, A. Klein, W. Jaegermann, P. Colson, C. Henrist, R. Cloots, Influence of ZnO surface modification on the photocatalytic performance of ZnO/NiO thin films, Catal. Lett. 149 (2019) 1813–1824, https://doi.org/10.1007/s10562-019-02781-z.

[52] A. Kotta, E.-B. Kim, S. Ameen, H.-S. Shin, H.K. Seo, Communication—ultra-small NiO nanoparticles grown by low-temperature process for electrochemical application, J. Electrochem. Soc. 167 (2020) 167517, https://doi.org/10.1149/1945-7111/abcf51.

[53] A.D. Arulsamy, K. Elersič, M. Modic, U. Cvelbar, M. Mozetič, Reversible carrier-type transitions in gas-sensing oxides and nanostructures, Chemphyschem 11 (2010) 3704–3712, https://doi.org/10.1002/cphc.201000572.

[54] Z. Yuan, Q. Zhao, Z. Duan, C. Xie, X. Duan, S. Li, Z. Ye, Y. Jiang, H. Tai, Ag2Te nanowires for humidity-resistant trace-level NO2 detection at room temperature, Sens. Actuators B Chem. 363 (2022) 131790, https://doi.org/10.1016/j.snb.2022.131790.

application of Pd sensitized heterojunction n-ZnO/p-NiO nanostructures, J. Alloys. Compd. 797 (2019) 456–464, https://doi.org/10.1016/j.jallcom.2019.05.111.

[55] Q. Zhao, W. Zhou, M. Zhang, Y. Wang, Z. Duan, C. Tan, B. Liu, F. Ouyang, Z. Yuan, H. Tai, Y. Jiang, Edge-Enriched Mo2TiC2Tx/MoS2 heterostructure with coupling interface for selective NO2 monitoring, Adv. Funct. Mater. 32 (2022) 2203528, https://doi.org/10.1002/adfm.202203528.

[56] L. Zhu, W. Zeng, Room-temperature gas sensing of ZnO-based gas sensor: a review, Senso. Actuators A Phys. 267 (2017) 242–261, https://doi.org/10.1016/j. sna.2017.10.021.

[57] J. Xuan, G. Zhao, M. Sun, F. Jia, X. Wang, T. Zhou, G. Yin, B. Liu, Low-temperature operating ZnO-based NO 2 sensors: a review, RSC Adv. 10 (2020) 39786–39807, https://doi.org/10.1039/D0RA07328H.

[58] R.K. Sonker, S.R. Sabhajeet, S. Singh, B.C. Yadav, Synthesis of ZnO nanopetals and its application as NO2 gas sensor, Mater. Lett. 152 (2015) 189–191, https://doi. org/10.1016/j.matlet.2015.03.112.

[59] A. Nagar, A. Kumar, U. Tyagi, H. Dhasmana, M.M. Khan, S. Husain, A. Verma, V. K. Jain, Ultrafast, trace-level detection of NH3 gas at room temperature using hexagonal-shaped ZnO nanoparticles grown by novel green synthesis technique, Physica B Condens. Matter 626 (2022) 413595, https://doi.org/10.1016/j. physb.2021.413595.

[60] M. Hjiri, F. Bahanan, M.S. Aida, L. El Mir, G. Neri, High Performance CO gas sensor based on ZnO nanoparticles, J. Inorg. Organomet. Polym. 30 (2020) 4063–4071, https://doi.org/10.1007/s10904-020-01553-2.

[61] J.F. Chang, H.H. Kuo, I.C. Leu, M.H. Hon, The effects of thickness and operation temperature on ZnO: Al thin film CO gas sensor, Sens. Actuators B Chem. 84 (2002) 258–264, https://doi.org/10.1016/S0925-4005(02)00034-5.